

<https://doi.org/10.1038/s41528-024-00308-0>

Water-based direct photopatterning of stretchable PEDOT:PSS using amphiphilic block copolymers

Check for updates

Soon Joo Yoon¹, Jeongdae Ha², Hyeokjun Lee², Jin Tae Park¹, Bin Hyung Lee³, Kyung-In Jang^{2,4,5}, Anna Yang⁶ & Yoon Kyeong Lee^{1,3,4} ✉

The use of water-based chemistry in photolithography during semiconductor fabrication is desirable due to its cost-effectiveness and minimal environmental impact, especially considering the large scale of semiconductor production. Despite these benefits, limited research has reported successful demonstrations of water-based photopatterning, particularly for intrinsically water-soluble materials such as Poly(3,4-ethylenedioxythiophene):poly(styrene sulfonate) (PEDOT:PSS) due to significant challenges in achieving selective dissolution during the developing process. In this paper, we propose a method for the direct patterning of PEDOT:PSS in water by introducing an amphiphilic Poly(ethylene glycol)-block-poly(propylene glycol)-block-poly(ethylene glycol) (PEO-PPO-PEO, P123) block copolymer to the PEDOT:PSS film. The addition of the block copolymer enhances the stretchability of the composite film and reduces the hydrophilicity of the film surface, allowing for water absorption only after UV exposure through a photoinitiated reaction with benzophenone. We apply this technique to fabricate tactile and wearable biosensors, both of which benefit from the mechanical stretchability and transparency of PEDOT:PSS. Our method represents a promising solution for water-based photopatterning of hydrophilic materials, with potential for wider applications in semiconductor fabrication.

Poly(3,4-ethylenedioxythiophene):poly(styrene sulfonate) (PEDOT:PSS) is considered to be one of the most promising conductive polymers due to its adjustable electronic properties, optical transparency, solution processability, and biocompatibility¹. PEDOT:PSS has demonstrated several key advantages that have facilitated its use in flexible and stretchable electronics, electrochemical transistors and sensors, energy storage, and tissue engineering². Over the past two decades, various compositions, doping techniques, and chemical modifications have been developed to meet the diverse requirements of different applications^{3,4}.

An aqueous dispersion of PEDOT:PSS is amenable to diverse solution-based manufacturing processes, including coating (e.g., dip-, spin-, and spray-coating) and printing (e.g., inkjet and screen printing)⁵⁻⁹. Among these techniques, photolithography stands out as a promising processing approach, which is instrumental in creating micro- or nanoscale structures on planar substrates¹⁰. Given the immense potential of PEDOT:PSS in

future electronic systems, devising chemistry for the photopatterning of PEDOT:PSS is critical to enabling reliable and scalable production of its potential applications. Several methods, such as reactive ion etching based on oxygen plasma with polymer masks, ion beam lithography, and electron beam lithography, have been explored to pattern PEDOT:PSS^{11,12}. However, direct patterning of PEDOT:PSS films without the need for overlay coating for selective masking has not been reported.

This paper presents a photopatterning process for the fabrication of transparent and stretchable conductive polymer composed of PEDOT:PSS. The surface hydrophobicity of the film is regulated by the addition of an amphiphilic Poly(ethylene glycol)-block-poly(propylene glycol)-block-poly(ethylene glycol) (PEO-PPO-PEO, P123) based block copolymer, which generates a phase-separated vertical structure through the hydrophobic-hydrophilic interaction with PEDOT:PSS¹³. Exposure to UV light triggers the chain scission of the block copolymer through

¹Department of Nano Convergence Engineering, Jeonbuk National University, Jeonju 54896, Republic of Korea. ²Department of Robotics Engineering, Daegu Gyeongbuk Institute of Science and Technology, Daegu 42988, Republic of Korea. ³Division of Advanced Materials Engineering, Jeonbuk National University, Jeonju 54896, Republic of Korea. ⁴ENSIDE Corporation, Daegu 42988, Republic of Korea. ⁵Korea Brain Research Institute, Daegu 41062, Republic of Korea.

⁶Department of Chemistry and Biochemistry, Swarthmore College, Swarthmore, PA 19081, USA. ✉ e-mail: yoonklee@jbnu.ac.kr

photoactivated benzophenone (BP), resulting in increased water wettability of the composite film and dissolution of the UV-exposed area. Demonstration of this technique involves the creation of transparent and stretchable touch sensors as well as wearable biosensors. This study highlights a promising approach for the development of conductive polymer-based devices with enhanced functionality while simultaneously addressing environmental concerns and cost-effectiveness in their production.

Results and discussion

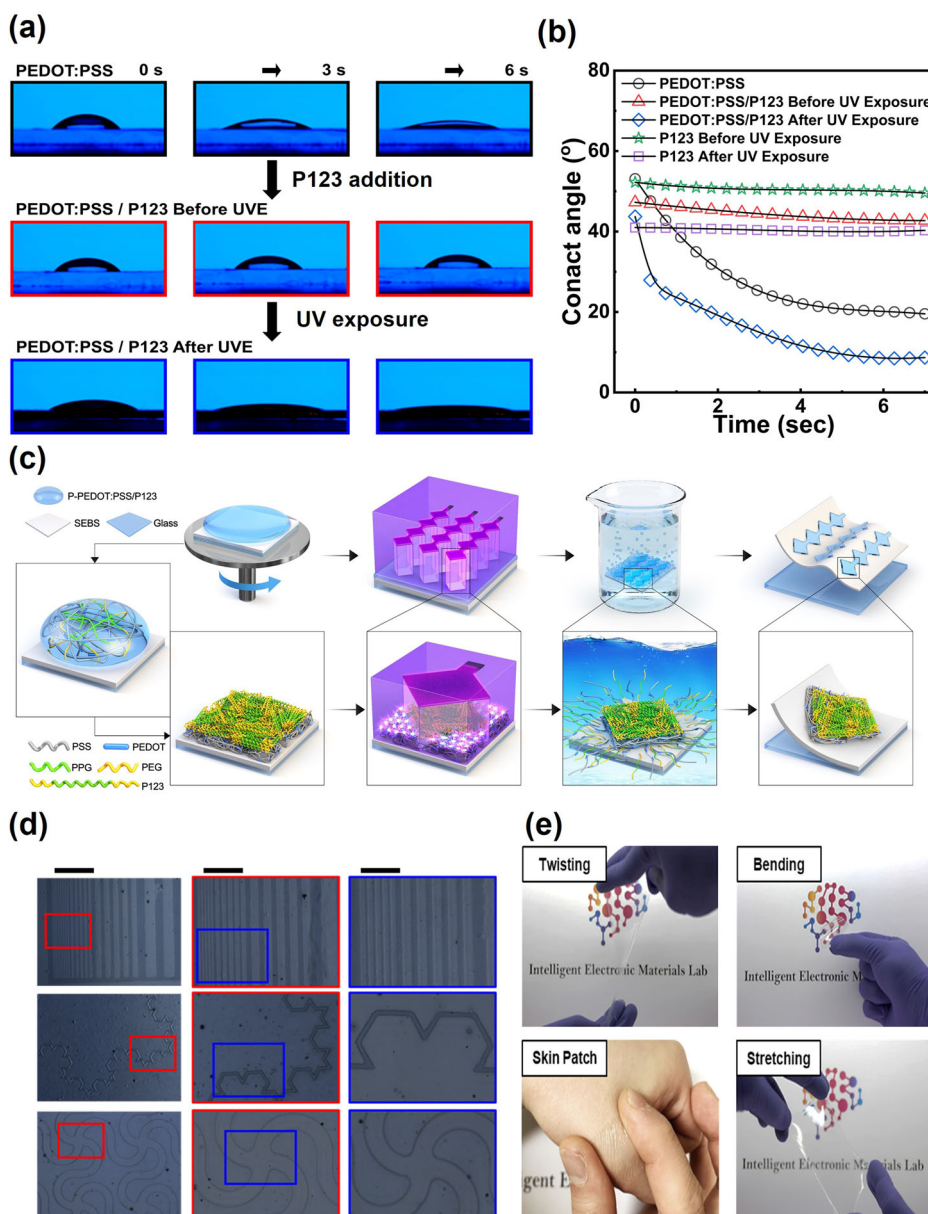
Patterning mechanism of Photopatternable PEDOT:PSS

Figure 1a shows the rapid decrease in the contact angle of water on the surface of PEDOT:PSS film due to its hydrophilicity. PEDOT is a conjugated polymer that can be oxidized to a positively charged conductive state. PSS contains negative charges as a result of deprotonated sulfonfyl groups and acts as a counterion to balance the positive charges of PEDOT¹⁴. When unmixed with other polymers, the secondary structure of PEDOT:PSS is composed of short, positively charged PEDOT chains that are electrostatically attached to the longer, negatively charged PSS chains¹⁵. PEDOT:PSS is highly water soluble forming colloidal particles with a

hydrophobic PEDOT-rich core and a hydrophilic PSS-rich shell¹⁶. Further aggregation of PEDOT cluster occurs upon water evaporation during the solid film formation resulting in multilayer stacks of PSS-encased PEDOT cores¹⁷. The cohesive strength between the aggregates originates from hydrogen bonding between the sulfonic acid groups of PSS and π -orbital stacking between PEDOT chains¹⁸. The high water solubility of PEDOT:PSS, however, poses a challenge for photopatterning using water as a developer^{19,20}. The microstructure of the PEDOT:PSS film also does not support stable conductivity under tensile stain due to the isolation of the conduction pathways upon stretching¹⁹.

The addition of poly(ethylene oxide)-poly(propylene oxide)-poly(ethylene oxide) (PEO-PPO-PEO) block copolymers, which are commercially available amphiphiles (known as Pluronic or Poloxamers), can modify the secondary and ternary structure of PEDOT:PSS in both water and solid state films²¹. A previous study reported that the interaction between Pluronic and PEDOT:PSS alters the electrical conductivity and stretchability of the PEDOT:PSS films due to the more linearized conformation of both polymers²¹. The study showed that the film achieved high electrical conductivity ($\sim 1700 \text{ S cm}^{-1}$) and minimal change in resistance

Fig. 1 | Process and patterned features of photo-patternable PEDOT:PSS. **a** Water contact angles depending on the film composition and UV exposure. After addition of P123 in the film composite, wetting occurs only after UV exposure. **b** Change of contact angles. **c** Photopatterning process of PEDOT:PSS. The UV-exposed area becomes soluble in water within 10 s. **d** Stereomicroscope images of patterned PEDOT:PSS films. The scale bar lengths from the left are 1000, 500, and 200 μm . **e** Images of PEDOT:PSS films on the SEBS substrate that show transparency and stretchability.



under 40% tensile strain²¹. In this study, a long PPO chain of the P123 version of Pluronics (PEO:PPO:PEO = 20:70:20) plays a critical role in controlling the water solubility of the PEDOT:PSS/P123 composite film. When P123 is blended with PEDOT/PSS in an aqueous medium and subsequently dried to generate a solid film, the composite film displays a relatively hydrophobic surface, as evidenced by the larger contact angle of approximately 50 degrees as shown in the second-row images of Fig. 1a. The modest variations observed in the contact angle, over a timescale of roughly 10 s (red line in Fig. 1b) indicate that the surface wetting of the composite film is significantly impeded compared to the pure PEDOT:PSS film, owing to the modified surface groups of the composite film.

In order to selectively dissolve the composite film in water for patterning, a photoactive compound, benzophenone (BP), was incorporated into the PEDOT:PSS/P123 composite film with a concentration of 1.6 wt%. The inclusion of benzophenone did not significantly alter the contact angle of the pristine films prior to UV exposure. All the data presented in Fig. 1 were obtained with BP. Compared to the negligible alterations in contact angle of the pure P123 film after UV exposure, a discernible decrease in contact angle manifested in the PEDOT:PSS/P123 film following UV exposure. The difference originates from the presence of a PEDOT:PSS layer under P123 in the composite film since the underlying PEDOT:PSS layer functions as an absorber of water diffused through the pores in UV-treated P123 (Supplementary Fig. 1). This phenomenon facilitates the dissolution of the PEDOT:PSS layer, serving as the impetus for the subsequent lift-off of the superimposed P123 layer. Detailed analytical simulations and chemical characterization will be provided in subsequent sections.

This pronounced contrast in hydrophilicity, depending on UV exposure, can facilitate the direct photopatterning of the composite film upon subsequent immersion in deionized water. Figure 1c describes the process of water-based patterning of the stretchable, conductive polymer that involves a UV-induced chemical change in the PEDOT:PSS/P123 composite film. The fabrication begins from the spin-coating of a mixture comprising PEDOT:PSS, P123, and benzophenone dissolved in a solution consisting of a 4 to 1 ratio of PEDOT:PSS aqueous solution and ethanol. After the solvent evaporation, conventional photolithography selectively exposes specific regions of the solid-state film. The exposed portion is subsequently dissolved in deionized water, functioning as a positive photoresist. The water-based, direct patterning of PEDOT:PSS/P123 avoids hazardous chemicals typically encountered in photoresist overlays or developers.

The optical images in Fig. 1d illustrate micropatterns achieved through the direct patterning of PEDOT:PSS/P123 films on a stretchable substrate under optimized photolithography conditions. The specific sample compositions and detailed procedures employed are outlined in the Methods section. The line patterning attains a minimum resolution of approximately 20 μm , with well-defined round and sharp edges. The serpentine patterns, commonly utilized for stretchable electrodes, exhibit a width of 50 μm , as exemplified in the last row of Fig. 1d. Figure 1e shows the images of stretchable PEDOT samples on a stretchable substrate, showcasing various deformation modes. Approximately 80% of the substrate surface is covered by diamond shaped PEDOT electrodes, illustrating both their stretchability and optical transparency.

The vertical distribution of component polymers in the PEDOT:PSS/P123 composite film can be investigated using X-ray photoelectron spectroscopy (XPS) of the solid film due to the distinct ratio between the C-H and C-O-C carbon 1s peaks, located at 284.5 eV and 286 eV, respectively²². Figure 2a shows that the pure P123 film exhibits a relatively larger C-O-C peak at 286 eV (highlighted in purple) in comparison to the lower binding C-H peak around 284.5 eV (highlighted in green). On the other hand, the pure PEDOT:PSS film displays a C-O-C peak smaller than a C-H peak, which contradicts the aforementioned intensity ratio between the two carbon peaks in P123. The XPS spectra acquired from the composite film show a relative intensity that is similar to P123, suggesting that the surface is P123-rich. The depth profile of the XPS data in Fig. 2b reveals that the film etching exposes the PEDOT:PSS-rich bottom layer, which exhibits a dominant C-H peak at 284.5 eV. The results suggest that PEDOT:PSS

precipitates first owing to the robust π - π interaction and hydrophobic properties of ethylenedioxy groups, forming PEDOT:PSS-rich bottom and P123-rich top layers²³.

Additional characterization of the UV-treated samples was conducted using XPS (Fig. 2a, lower row) and Fourier-transform infrared spectroscopy (FT-IR, Supplementary Fig. 2). These analyses reveal the origin of the observed changes in hydrophilicity induced by UV treatment. Specifically, the carbon XPS peaks of P123 and PEDOT:PSS/P123 samples exhibit the emergence of new C=O bonds, highlighted in red, at a binding energy of around 289 eV. The peak intensity corresponding to the ether bond (C-O-C) at around 286 eV (purple) decreased following UV exposure. Such changes were observed only for the films that contained both P123 and BP. However, no significant changes were observed for the PEDOT:PSS/BP film without P123, as depicted in the middle column of the graphs in Fig. 2a.

Solution nuclear magnetic resonance (NMR) was attempted to further investigate the details of the UV-induced chemical change. Solution NMR provided limited chemical information, however, due to the formation of insoluble film after UV exposure, which remained insoluble in water, DMSO, acetone, or toluene. The insoluble fragmented films generated by UV exposure are lifted off by the water absorption to the underlying PEDOT and its subsequent dissolution. The NMR samples included only the soluble portion of the UV-treated samples after filtering the insoluble portion. Broadband ¹³C-NMR (Supplementary Fig. 3) showed five new peaks at 146, 129, 126, 125.6, and 83 ppm after UV exposure, corresponding to the reduced benzophenone. However, the peak at 83 ppm did not appear in the distortionless enhancement by polarization transfer (DEPT)-90/135 ¹³C-NMR, suggesting that it is the quaternary carbon. This observation indicates that the ketyl radical can react with other radicals generated in P123 (Path I in Fig. 2c) or terminate to give benzopinacol (Path II). Hydrogen abstraction to form ketyl radicals could occur in various chains in P123, such as -CH₂, -CH, and -OH. Although possible to form radical on PEO chains, it is most likely that hydrogen abstraction to occur in PPO due to the more stable tertiary radical that can be formed on the PPO chains.

Reaction pathway III in Fig. 2c summarizes comprehensive potential mechanisms that can occur for P123 subsequent to hydrogen abstraction from benzophenone. The formation of an insoluble film and C=O bonds due to UV exposure suggests both the scission of ether bond and cross-linking on the P123-dominant film surface. The reaction pathway III-1 in Fig. 2c illustrates the crosslinking between P123 polymer chains. The insoluble film layer formed after UV exposure is suspected to be cross-linked high molecular weight polymers. An alternative pathway III-2 yields smaller fragments with carbonyl groups, consistent with the changes in carbon peaks observed in XPS data. It is also plausible that small molecules such as 1,2-propanediol, acetic acid, and formic acid may form via photo-oxidative fragmentation of P123 in the presence of water and air, similar to the process observed in the thermal oxidative fragmentation²⁴. These hydrophilic small molecules and the possible formation of carboxylic acid (Path III-2') are suspected to be responsible for the dewetting of the composite film after UV exposure when the patterns were formed on a hydrophobic surface treated with APTES (Supplementary Fig. 4).

A finite element analysis in Fig. 3 simulates water penetration into the composite film to explain the remarkable increase in hydrophilicity of PEDOT:PSS/P123 film after UV exposure. It is notable that the UV-induced dissolution of the composite film only occurs in the presence of the PEDOT:PSS bottom layer. To achieve simulation results in accordance with this experimental observation, specific parameters related to water uptake were estimated by fitting experimental data on water uptake. Assuming the water droplets employed for contact angle measurements adopt the configuration of a spherical cap, the absorbed water mass can be computed by utilizing the initial droplet volume in conjunction with the contact angle data observed over time. Simulation parameters include the diffusion coefficients (*D*) and

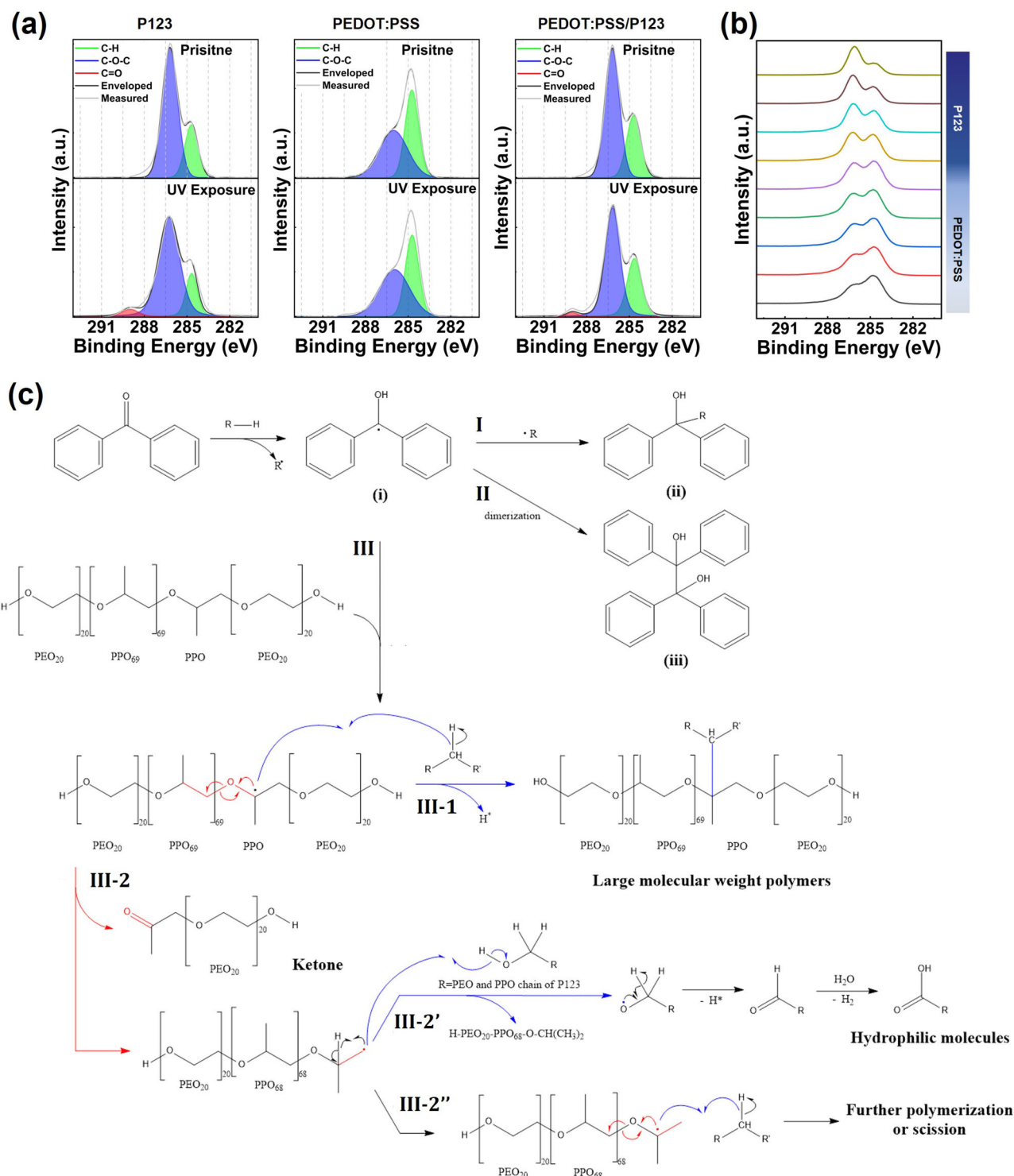


Fig. 2 | Patterning Mechanism of Photopatternable PEDOT:PSS. **a** The change of carbon peaks before and after UV exposure. The C=O bonds (red) emerge from the photoactivated process of P123. **b** Depth profile of carbon XPS peaks that reveal the P123-rich surface and PEDOT:PSS-rich bottom layers inside the composite film.

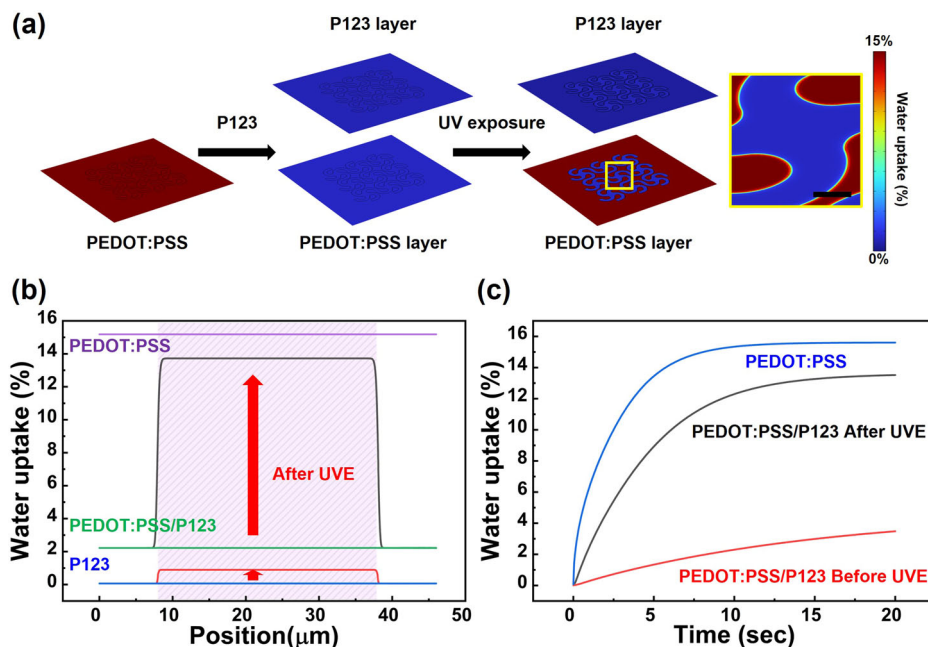
c Proposed chemical mechanism of hydrophilicity control after UV exposure. Chemical reactions initiated by the photoactivated benzophenone and ensuing chain cleavage of P123.

water absorption capacities (S) for the PEDOT:PSS and P123-rich layers before and after UV exposure. Details of the methods and estimated values of the parameters are described in Supplementary Text 1, Supplementary Fig. 5, and Supplementary Table 1. While the water absorption capacity of P123 remain similar before and after UV exposure, the diffusion coefficient of the P123-rich layer increased significantly after UV exposure (9.0 to $14.7 \times 10^{-16} \text{ m}^2 \text{ s}^{-1}$). This tendency of the P123-rich layer enabled the

selective dissolution of the underlying PEDOT:PSS layer, thereby facilitating the patterning process.

Figure 3a illustrates the distribution of water for three different films (PEDOT:PSS film, PEDOT:PSS/P123 composite films before and after UV exposure) when immersed in water for 10 s. For the pure PEDOT:PSS film, water permeates throughout the entire area, resulting in complete soaking. Water permeation into the composite film is effectively inhibited before UV

Fig. 3 | Finite Element Analysis for Water Uptake in Composite Films. **a** Distribution of water absorption for PEDOT:PSS and P123/PEDOT:PSS films before and after UV exposure after 10 s of water exposure. The structure of the composite films was modeled as double layers with P123 top and PEDOT bottom layers. **b** Water mass fraction depending on the film composition at 10 s after UV exposure. Lateral positions between ~ 8 and $38 \mu\text{m}$ were assumed to be exposed to UV. **c** Total water uptake as a function of soaking times depending on the film composition and UV exposure.



exposure, however, allowing only scant water penetration into the underlying PEDOT:PSS layer due to the small value of the diffusion constant of the P123 top layer. When certain regions of the composite film are exposed to UV, water penetrates into the PEDOT:PSS layer only within the areas under the UV-exposed P123, while negligible water absorption occurs within the regions shielded by unexposed P123. The P123-rich layer exhibits a small amount of water absorption over the simulation time due to its intrinsically low water absorption capacity. This implies that the P123-rich layer predominantly functions as a conditional pathway for water penetration.

Figure 3b and Supplementary Fig. 6 depict the mass fraction of water as a function of the lateral location of the films. The shaded regions represent the areas exposed to UV irradiation. Water penetrates uniformly for the pure PEDOT:PSS film and the composite film before UV exposure. When the middle area between 8 and $38 \mu\text{m}$ is subjected to UV exposure, a significant increase in water mass fraction is observed for the composite film. A steep gradient emerges at the boundary demarcating UV-exposed regions, ensuring a reliable patterning process.

Figure 3c illustrates the water uptake rates of the three films. In the PEDOT:PSS film, water uptake nearly reaches saturation within a brief span of $3\text{--}4$ s due to its high diffusion coefficient. For the composite film, the presence of the P123-rich layer impedes the diffusion of water, resulting in a comparatively gradual progression of water uptake. Notably, a distinct contrast in water uptake rate is observed in the composite film before and after UV exposure. The slow water uptake rate before UV exposure is remarkably accelerated upon exposure to UV radiation. The simulation results show that UV-induced change in the water absorption dynamics of the P123-rich layer enables the selective absorption of a substantial volume of water exclusively in areas subjected to UV irradiation. Consequently, this methodology facilitates deterministic patterning of PEDOT:PSS/P123 layers in water with a brief immersion time of approximately 10 s.

Optical and mechanical properties of patterned PEDOT:PSS

Figure 4 summarizes the optical transparency and mechanical stretchability of the composite films. The stretchability of the pristine film is enhanced through the dehydration cross-linking reaction of P123, achieved via sulfuric acid treatment^{25–27}. This process not only contributes to increased stretchability but also facilitates the formation of sizable PEDOT domains, resulting in improved electrical conductivity²¹. The synergistic effect of these mechanisms enhances the overall performance of the film, making it

simultaneously more stretchable and electrically conductive compared to its untreated counterpart. The sheet resistance of the film was reduced by $\sim 56\%$ after the acid treatment, as shown in Supplementary Fig. 8. The transmittance values at a wavelength of 575 nm were determined to be 94% , 92% , and 88% for the pristine, H_2SO_4 -treated, and BP-contained samples, respectively. The decline in transmittance, specifically in the long wavelength region exceeding 600 nm , is ascribed to the formation of high molecular weight P123 chains resulting from the P123 dehydration cross-linking reaction during the sulfuric acid treatment^{28–31}.

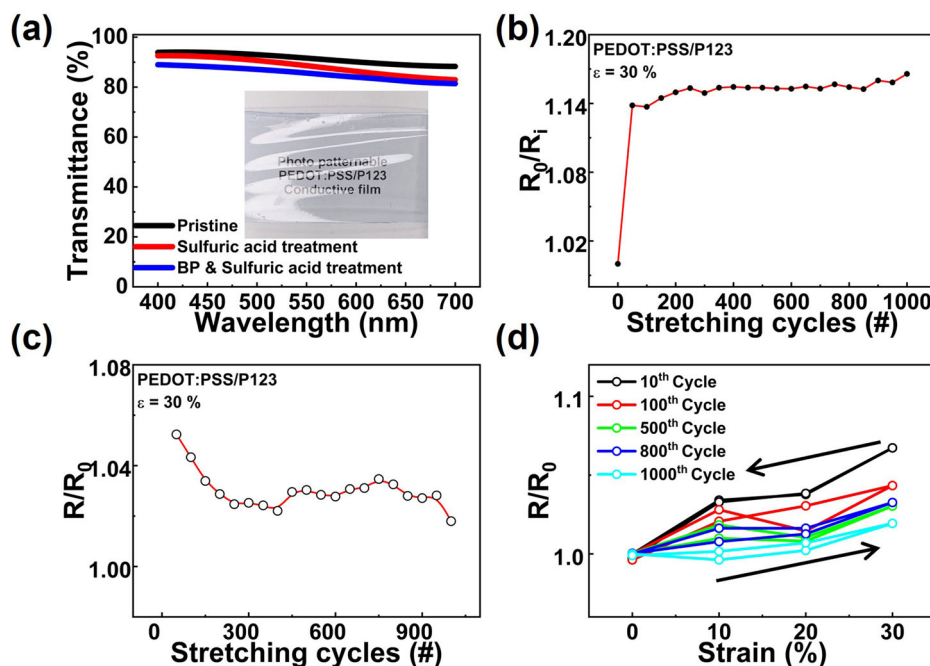
The mechanical endurance of the fabricated photopatternable PEDOT:PSS/P123 electrodes was assessed under conditions of cyclic stretching and releasing between 0 and 30% tensile strains after sulfuric acid treatment (Fig. 4b–d). Herein, R_i , R_0 , and R represent the resistances of initial states before the cycles, unstrained states ($\epsilon = 0\%$), and stretched states ($\epsilon = 30\%$) during the cycle, respectively. R_0 increased about 14% after the initial cycle and displayed a 3% increase during the following 1000 cycles. Meanwhile, the resistance at $\epsilon = 30\%$ (R , Fig. 4c) demonstrated minor fluctuations of 5% or less over the course of 1000 cycles. The resistance variations depicted in Fig. 4b, c decreased with repetitive cycling, attributed to the change in the dimensions of PEDOT cores over successive strain cycles³².

Application of Photopatternable PEDOT:PSS in a wearable device

Figure 5 illustrates the practical realization of a stretchable and transparent capacitive touch sensor utilizing a photopatternable PEDOT:PSS/P123 film. The schematic representation of the device configuration is presented in Fig. 5a. The substrate and dielectric layer were fabricated using SEBS, chosen for its remarkable stretchability and optical transparency. The diamond-shaped patterns of PEDOT:PSS/P123 electrode were incorporated to enhance the device capacitance. Detailed information regarding the layer thicknesses and electrode dimensions can be found in the experimental section.

The capacitive behavior of the touch sensor is depicted in Fig. 5b. When a finger approaches the sensor surface, fringing electric fields between adjacent diamond-patterned electrodes become reduced³². Upon physical contact, a discernible change in capacitance (ΔC) of 0.12 pF was observed from the baseline capacitance of 1.02 pF . Capacitance decreases measured at non-contact distances from 1 cm to 5 cm imply potential applicability as a proximity touch sensor. The touch sensor reliably reverts to its initial capacitance upon finger removal, validating its operational reversibility.

Fig. 4 | Optical and Electrical Properties of PEDOT:PSS/P123 Films. **a** Transmittance of the PEDOT:PSS film on SEBS for the wavelength in a visible range. **b** Change of resistance at 0% strain (R_0) during the stretching cycles normalized by the initial value before the stretching cycles (R_i). **c**, **d** Change in resistance under 30% strain (R) normalized by the resistance at 0% strain (R_0) at each cycle. **d** Hysteresis of normalized resistance (R/R_0) during the stretching cycles.



The device resilience to mechanical deformations was assessed through tensile and bending tests, as shown in Fig. 5c, d. Up to 40% uniaxial strain, the capacitance uniformly increases due to the reduced thickness of the dielectric layer and larger electrode size. When subjected to uniaxial stretching above 40%, the capacitance decreases by $\sim 12\%$ due to the expanding dielectric length between the diamond-patterned electrodes. Under bending deformation of the sensor (Fig. 5d), a baseline capacitance of 1.02 pF and post-touch capacitance of 0.74 pF remain stable until a bending radius of 6 mm. The increase in capacitance observed below a bending radius of 6 mm is attributable to the sensor's deformation under pronounced bending conditions. The lower position of the neutral plane originating from the thick substrate causes the expansion of the electrode areas and diminishes the gap between the upper and lower electrodes³³. Additionally, the change in the parasitic capacitance between the lower electrodes and the surrounding air at smaller bending radii can increase the overall capacitance^{33–35}.

To assess the feasibility of the photopatternable PEDOT electrodes in wearable technology, electrooculogram (EOG), electrocardiogram (ECG), and electromyogram (EMG) sensors were developed. Supplementary Figure 9 depicts the electrochemical impedance spectroscopy (EIS) analysis to assess the contact impedance of the stretchable PEDOT:PSS/P123 electrode with the skin. To minimize motion artifacts during the data acquisition process, the three electrodes (reference, counter, working electrode) were affixed to the skin surface of the thigh and secured using tape to mitigate potential interference from concurrent physiological electrical signals, such as respiration, muscle movement, and electrocardiogram (ECG) signals³⁶.

For EOG signal acquisition, electrodes were strategically positioned around the eyes as illustrated with black circles in Fig. 5e. High transmittance characteristics of the sensor electrodes made the mounted devices scarcely noticeable (Fig. 5f). Specifically, a pair of sensors were situated above and below the eyebrows to capture vertical eye movements. The reference electrode was placed on the zygomatic bone adjacent to the eye, with the + and – electrodes connected to the upper and lower eye sensors, respectively. The schematic and experimentally measured EOG signals are depicted in the left and right graphs of Fig. 5g, respectively. In EOG, positive corneal potentials are detected by the nearer electrode during gaze shifts toward it, while negative retinal potentials are collected by the distant electrode. Consequently, an upward gaze yields a positive potential, whereas a downward gaze results in a negative potential³⁷. The magnitude of the

recorded EOG signal through the sensor was measured to be 13.8 ± 0.4 mV in the vertical dimension, showcasing a noticeable voltage alteration with each eye movement.

In a similar manner, ECG signals were acquired using the same electrode configuration as the EOG sensor with the mounting locations indicated by the red circles in Fig. 5e. The ECG waveforms encompass distinct components such as P, Q, R, S, and T waves depending on the cardiac cycles³⁸. Heart rate calculations derived from the reciprocal of the time between R waves yielded a measurement of 71.4 beats per minute (bpm), confirming the device reliability in this context.

The acquisition of EMG signals was attempted for their increasing prominence in various applications such as skeleton robot control or prosthetics. In this application, the reference electrode was affixed to the elbow, while the + and – electrodes were attached to the flexor digitorum profundus and extensor digitorum, respectively, to detect electrical signals produced during clenching and releasing hand gestures. In EMG signal measurements, the voltage differential between clenching and releasing hand motions was approximately 70 mV, facilitating clear differentiation between the two actions (Fig. 5i).

In conclusion, this study successfully developed a straightforward and environmentally friendly photolithography technique by incorporating the amphiphilic polymer P123 and benzophenone as a photoinitiator into the conductive polymer PEDOT:PSS. The related chemistry enabled the formation of patterns with a minimum line width of 20 μm in water. The patterning mechanism of PEDOT:PSS/P123 was elucidated through a comprehensive analysis, including XPS and finite element analysis (FEA) simulations. The patterned PEDOT:PSS/P123 demonstrated a stretchable and transparent touch sensor due to its elasticity and transmittance. The electrodes also successfully captured essential biosignals such as EOG, ECG, and EMG. The results demonstrated significant promise of the photopatternable PEDOT:PSS for an ideal candidate for stretchable electronics and comfortable, visually unobtrusive skin patches, ensuring a seamless and convenient wearable experience without causing discomfort to users.

Methods

Materials

PEDOT:PSS (Clevios PH1000, PEDOT:PSS = 1 : 2.5, solids content : 0.77%) was purchased from Heraeus. Poly(ethylene glycol)-poly(propylene glycol)-poly(ethylene glycol) ($M_n = \sim 5800$, PEO-PPO-

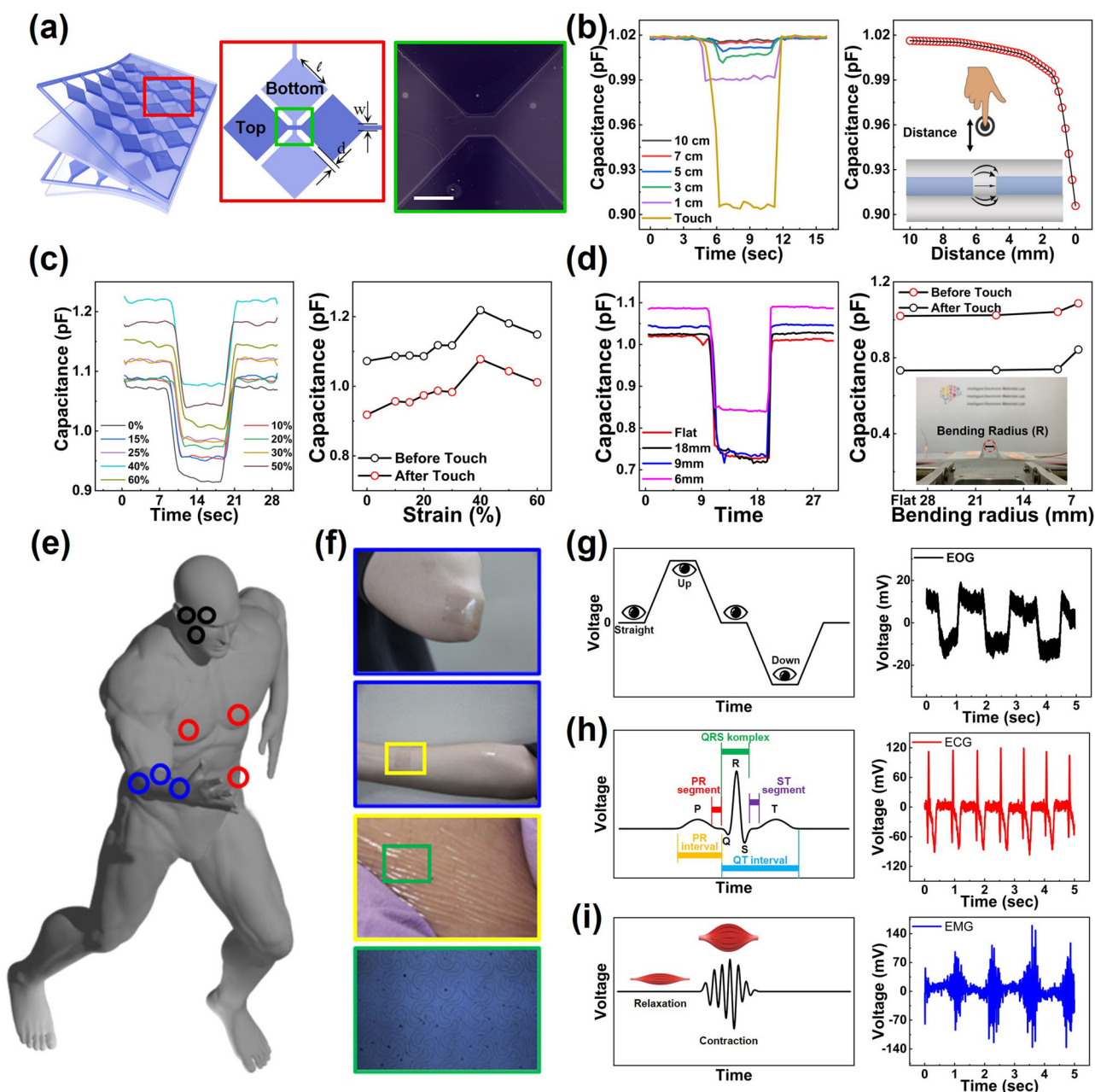


Fig. 5 | Electrical characteristics of the fabricated stretchable touch sensor and the measurement results obtained from the biosignal-detecting sensor. **a** Illustration of the diamond-patterned electrodes in a transparent and stretchable touch sensor. The scale bar length is 400 μm . **b** Capacitance change depending on the distance of the finger from the sensor surface. **c** Capacitance changes depending on the strain.

d Capacitance changes depending on the bending radius. **e** Positioning sites for EOG, ECG, and EMG sensors: black for EOG, red for ECG, and blue for EMG. **f** Optical images of the mounted EMG sensor and microscopic view of the sensor electrode patterns. **g–i** Plots of typical waveforms (left) and measured signals (right) from **g** EOG, **h** ECG, **i** EMG sensors.

PEO, P123), benzophenone (ReagentPlus, 99%), sulfuric acid (ACS reagent, 95.0–98.0%) were purchased from Sigma-Aldrich. Styrene-ethylene-butylene-styrene (SEBS, Tuftec H1052) was purchased from PHILJIN commercial.

Preparation of photopatternable PEDOT:PSS/P123 solution with benzophenone

PEDOT:PSS and P123 were stirred overnight at 900 rpm (P123 20 wt% in PEDOT:PSS) Benzophenone solution (10 wt% in ethanol) was added to the mixed solution and stirred at 1000 rpm for 2 h. The mixture was cooled to 5 °C. The finally mass ratio of the mixture was PEDOT:PSS solution : P123 : ethanol : benzophenone = 4 : 1 : 1 : 0.1.

Fabrication of transparent, stretchable touch sensor

A 400 mg per ml solution of SEBS dissolved in toluene was spin-coated at 500 rpm for 1 min on a 2.5 × 7 cm slide glass cleaned with acetone and IPA. The coated glass was annealed at 90 °C for 1 h on a hot plate. The glass/SEBS substrate was then treated with O₂ plasma with an oxygen flow rate of 10 sccm for 5 min. The photoinitiated PEDOT:PSS/P123 solution was spin-coated at 2000 rpm for 1 min on the surface-treated SEBS substrate, followed by prebaking at 110 °C for 1 min. The photoinitiated PEDOT:PSS/P123 was patterned under UV exposure (365 nm, MIDAS system, Republic of Korea) with intensity of 15 mW cm⁻² for 15 min through film combined glass mask, and then postexposure bake at 110 °C for 1 min. As a result, a specific pattern was formed through direct patterning, and then the area

exposed to UV was developed through DI water. Finally, The patterned PEDOT:PSS film was baked on a hot plate at 60 °C for 1 h. Multilayer SEBS/PEDOT:PSS/P123 films were obtained by repeating the previous steps. The geometric specifications include a diamond-patterned electrode size (P) of 36 mm² (6 mm by 6 mm), a distance between the top and bottom diamond-shaped electrodes (d) of 54 μm, and a bridge width of 200 μm in this electrode arrangement. The thickness of the dielectric layer between the top and bottom electrodes is 20 μm.

Characterizations of photopatternable PEDOT:PSS/P123 films

Optical microscope images were acquired using a stereo microscope to facilitate the examination of the PEDOT:PSS/P123 material produced through direct patterning. Transmittance measurements of the PEDOT:PSS/P123 film within the visible light spectrum were performed utilizing UV–vis spectroscopy. The sheet resistance of the synthesized composite thin film was quantified employing a 2400 sourcemeter (Keithley, USA) in conjunction with a 4-point probe station.

Mechanical analysis of the SEBS/PEDOT:PSS/P123 hybrid material encompassed assessments of Young's modulus and yield strength, executed via a universal testing machine (Shimadzu, Japan). Evaluations concerning the response of transparent, stretchable electrodes to mechanical deformations were carried out employing a Keithley 4200 semiconductor characterization system (Keithley, USA) and a uniaxial tensioner. Additionally, an investigation into the touch sensor characteristics across a spectrum of deformations was conducted.

NMR spectroscopy

Solution-state proton (¹H) and carbon-13 (¹³C) nuclear magnetic resonance (NMR) spectra of P123 were acquired using a 600 MHz FT-NMR spectrometer installed in the Center for University-wide Research Facilities (CURF) at Jeonbuk National University. P123 samples, both pre- and post-UV treatment, underwent complete removal of residual moisture and solvents through a lyophilization process lasting 24 hours. The preparation of P123 solutions in dimethyl sulfoxide (DMSO-d₆) was followed by the removal of insoluble constituents via centrifugation at 4000 rpm for 10 min. Chemical shifts were referenced against the carbon resonances of DMSO-d₆.

XPS analysis

X-ray photoelectron spectroscopy (XPS) was conducted to scrutinize the composition of PEDOT:PSS, P123, and PEDOT:PSS/P123 composite mixtures. X-ray photoelectron spectroscopy (XPS) depth profiling provides chemical distributions based on the disparities in the intensity of C–H and C–O–H peaks between the upper P123 and lower PEDOT layers. The investigations were carried out using a Nexa XPS system (ThermoFisher, UK) with an Al K α monochromatic X-ray source (energy: 1486.6 eV). The experiments were conducted under vacuum conditions of 1.0×10^{-7} Torr at room temperature.

In addition, depth profiling analysis was undertaken to explore the subsurface composition. To achieve this, the XPS analysis was repeated after subjecting the samples to 60 s of etching using a 4 keV per 500 clusters of Ar ions, facilitated by an Ar ion cluster integrated within the same XPS system.

Fourier-transform infrared

For Fourier-transform infrared (FTIR) analysis, the samples were meticulously prepared using the same conditions as those employed for the XPS analysis. The FTIR measurements were executed with a spectral resolution of 4 cm⁻¹, employing the attenuated total reflectance (ATR) mode. The analysis spanned a spectral range from 4000 to 650 cm⁻¹.

Finite element analysis

To analyze the phenomenon of water penetration into polymer films, simulation analyses were conducted using the widely utilized software COMSOL 6.5. A dense 2D and 3D mesh was generated, with a particularly high mesh density at the interfaces between the films. The Transport of

Diluted Species (TDS) model was employed, and weak inequality constraints were applied to each domain to ensure that the films did not contain concentrations exceeding their water absorption capacity limits. The normalization method was employed to avoid discontinuities in variables or divergence in concentration gradients at the heterogeneous interface (Supplementary Fig. 10)^{39,40}. Instead of using the water concentration as the dependent variable in the simulation, we used a variable normalized against the water absorption capacities of each polymer. This approach prevents discontinuities at the interface. After completing the simulation analysis, the normalized water concentration was calculated by multiplying the water absorption capacities of each polymer with the normalized variable^{39,40}. The diffusion characteristics were determined through the transport properties module. The analysis involved setting the maximum water concentration (S) at the interface between the polymer film in direct contact with water. The parameters used in the simulation were determined by utilizing the parameter estimation module to achieve the best fit with experimental data. The determined parameters are presented in Supplementary Table 1.

Parameter fitting

The relationship between the contact angle and the volume of the water droplet was approximately calculated. The water droplet was assumed to have the shape of a sphere cap. Simulation parameters were estimated to fit the calculated water uptake data over time with the simulation results. More details are provided in Supplementary Text 1.

Measurement of electrophysiological (EP) signals

For the measurement of the electrooculography (EOG) signal, three PEDOT:PSS-based electrodes were attached to the periphery of the right eye. The ground electrode was attached to the cheekbone next to the ear, and the other two electrodes were attached above and below the eye. Then, EOG was recorded by moving the eyes up and down without moving the facial muscles. The recorded data were digitized at 400 Hz, with an average filter (15 ms of length) to reduce the high-frequency noise from the EOG signal. ECG signal was recorded from three electrodes placed over the most medial areas of the left and right fourth intercostal spaces and left pelvic bone (ground electrode). The data also were collected at a sampling frequency of 400 Hz, with an average filter (15 ms of length) to eliminate the noise. For measurement of Electromyography (EMG), the ground electrode is attached to the lateral epicondyle bone, and the other two electrodes are located on the right arm (flexor carpi radialis). The ECG was recorded by repeatedly clenching and unclenching the fist, and the data also were digitized at 400 Hz, with an average filter (15 ms of length). The observed biosignals were obtained without supplementary electrolytic gels on the electrodes.

Data availability

The data that support the findings of this study are available on request from the corresponding author.

Received: 10 October 2023; Accepted: 22 March 2024;

Published online: 03 April 2024

References

- Ouyang, J. "Secondary doping" methods to significantly enhance the conductivity of PEDOT:PSS for its application as transparent electrode of optoelectronic devices. *Displays* **34**, 423–436 (2013).
- Groenendaal, L., Jonas, F., Freitag, D., Pielartzik, H. & Reynolds, J. R. Poly(3,4-ethylenedioxythiophene) and its derivatives: past, present, and future. *Adv. Mater.* **12**, 481–494 (2000).
- Ouyang, J. et al. On the mechanism of conductivity enhancement in poly(3,4-ethylenedioxythiophene):poly(styrene sulfonate) film through solvent treatment. *Polymer* **45**, 8443–8450 (2004).
- Fan, B., Mei, X. & Ouyang, J. Significant conductivity enhancement of conductive poly(3,4-ethylenedioxythiophene):poly(styrenesulfonate)

- films by adding anionic surfactants into polymer solution. *Macromolecules* **41**, 5971–5973 (2008).
5. Guo, Y. et al. PEDOT:PSS “Wires” printed on textile for wearable electronics. *ACS Appl. Mater. Interfaces* **8**, 26998–27005 (2016).
 6. Dijk, G., Ruigrok, H. J. & O’Connor, R. P. Influence of PEDOT:PSS coating thickness on the performance of stimulation electrodes. *Adv. Mater. Interfaces* **7**, 2000675 (2020).
 7. Zabih, F., Xie, Y., Gao, S. & Eslamian, M. Morphology, conductivity, and wetting characteristics of PEDOT:PSS thin films deposited by spin and spray coating. *Appl. Surf. Sci.* **338**, 163–177 (2015).
 8. Eom, S. H. et al. Polymer solar cells based on inkjet-printed PEDOT:PSS layer. *Org. Electron.* **10**, 536–542 (2009).
 9. Sinha, S. K. et al. Screen-printed PEDOT:PSS electrodes on commercial finished textiles for electrocardiography. *ACS Appl. Mater. Interfaces* **9**, 37524–37528 (2017).
 10. Ouyang, S. et al. Surface patterning of PEDOT:PSS by photolithography for organic electronic devices. *J. Nanomater.* **2015**, 1–9 (2015).
 11. Choi, J.-H. et al. Enhancement of organic solar cell efficiency by patterning the PEDOT:PSS hole transport layer using nanoimprint lithography. *Org. Electron.* **14**, 3180–3185 (2013).
 12. Charlot, B. et al. Micropatterning PEDOT:PSS layers. *Microsyst. Technol.* **19**, 895–903 (2013).
 13. Soni, S. S., Brotons, G., Bellour, M., Narayanan, T. & Gibaud, A. Quantitative SAXS analysis of the P123/water/ethanol ternary phase diagram. *J. Phys. Chem. B* **110**, 15157–15165 (2006).
 14. Kayser, L. V. & Lipomi, D. J. Stretchable conductive polymers and composites based on PEDOT and PEDOT. *Adv. Mater.* **31**, 1806133 (2019).
 15. Rivnay, J. et al. Structural control of mixed ionic and electronic transport in conducting polymers. *Nat. Commun.* **7**, 11287 (2016).
 16. Lang, U., Müller, E., Naujoks, N. & Dual, J. Microscopical investigations of PEDOT:PSS thin films. *Adv. Funct. Mater.* **19**, 1215–1220 (2009).
 17. Nardes, A. M. et al. Microscopic understanding of the anisotropic conductivity of PEDOT:PSS thin films. *Adv. Mater.* **19**, 1196–1200 (2007).
 18. Takano, T., Masunaga, H., Fujiwara, A., Okuzaki, H. & Sasaki, T. PEDOT nanocrystal in highly conductive PEDOT:PSS polymer films. *Macromolecules* **45**, 3859–3865 (2012).
 19. Lang, U., Naujoks, N. & Dual, J. Mechanical characterization of PEDOT:PSS thin films. *Synth. Met.* **159**, 473–479 (2009).
 20. Bießmann, L. et al. Monitoring the swelling behavior of PEDOT:PSS electrodes under high humidity conditions. *ACS Appl. Mater. Interfaces* **10**, 9865–9872 (2018).
 21. Lee, J. H. et al. Highly conductive, stretchable, and transparent PEDOT:PSS electrodes fabricated with triblock copolymer additives and acid treatment. *ACS Appl. Mater. Interfaces* **10**, 28027–28035 (2018).
 22. Du, F.-P. et al. PEDOT:PSS/graphene quantum dots films with enhanced thermoelectric properties via strong interfacial interaction and phase separation. *Sci. Rep.* **8**, 6441 (2018).
 23. Zhang, X., Yang, W., Zhang, H., Xie, M. & Duan, X. PEDOT:PSS: from conductive polymers to sensors. *Nanotechnol. Precis. Eng.* **4** (2021).
 24. Gallet, G., Erlandsson, B., Albertsson, A. C. & Karlsson, S. Thermal oxidation of poly(ethylene oxide-propylene oxide-ethylene oxide) triblock copolymer: focus on low molecular weight degradation products. *Polym. Degrad. Stab.* **77**, 55–66 (2002).
 25. Zhang, J. et al. Effects of tailoring and dehydrated cross-linking on morphology evolution of ordered mesoporous carbons. *RSC Adv.* **6**, 19515–19521 (2016).
 26. Li, L., Song, H. & Chen, X. Ordered mesoporous carbons from the carbonization of sulfuric-acid-treated silica/triblock copolymer/sucrose composites. *Microporous Mesoporous Mater.* **94**, 9–14 (2006).
 27. Tehrani, M. & Sarvestani, A. Effect of chain length distribution on mechanical behavior of polymeric networks. *Eur. Polym. J.* **87**, 136–146 (2017).
 28. Anders, U., Nuyken, O. & Buchmeiser, M. R. Influence of chain length and temperature on UV-vis absorption and degradation behavior of poly(diethyl dipropargylmalonate) with an alternating cis-trans-1,2-(cyclopent-1-enylene)vinylene structure. *Des. Monomers Polym.* **6**, 135–143 (2003).
 29. Zhou, C. et al. Chain Length Dependence of the Photovoltaic Properties of Monodisperse Donor–Acceptor Oligomers as Model Compounds of Polydisperse Low Band Gap Polymers. *Adv. Funct. Mater.* **24**, 7538–7547 (2014).
 30. Hayashi, S., Yamamoto, S. & Koizumi, T. Effects of molecular weight on the optical and electrochemical properties of EDOT-based π -conjugated polymers. *Sci. Rep.* **7**, 1078 (2017).
 31. Sears, W. M., MacKinnon, C. D. & Kraft, T. M. The effect of chain length on the dielectric and optical properties of oligothiophenes. *Synth. Met.* **161**, 1566–1574 (2011).
 32. Lee, Y.-Y. et al. Growth Mechanism of Strain-Dependent Morphological Change in PEDOT:PSS Films. *Sci. Rep.* **6**, 25332 (2016).
 33. Yoo, D., Won, D., Cho, W., Lim, J. & Kim, J. Double side electromagnetic interference-shielded bending-insensitive capacitive-type flexible touch sensor with linear response over a wide detection range. *Adv. Mater. Technol.* **6**, 2100358 (2021).
 34. Won, D.-J., Yoo, D. & Kim, J. Effect of a microstructured dielectric layer on a bending-insensitive capacitive-type touch sensor with shielding. *ACS Appl. Electron. Mater.* **2**, 846–854 (2020).
 35. Li, M., Liang, J. & Zhang, M. Unidirectional sensitive flexible sensor for bending measurements. *Curr. Appl. Phys.* **23**, 36–41 (2021).
 36. Castrillón, R., Pérez, J. J. & Andrade-Caicedo, H. Electrical performance of PEDOT:PSS-based textile electrodes for wearable ECG monitoring: a comparative study. *Biomed. Eng. Online* **17**, 38 (2018).
 37. Ameri, S. K. et al. Imperceptible electrooculography graphene sensor system for human–robot interface. *npj 2D Mater. Appl.* **2**, 19 (2018).
 38. Arafat, M. A. & Hasan, M. K. Automatic detection of ECG wave boundaries using empirical mode decomposition. in *2009 IEEE International Conference on Acoustics, Speech and Signal Processing* 461–464 (IEEE, 2009). <https://doi.org/10.1109/ICASSP.2009.4959620>.
 39. Ma, L., Joshi, R., Keith Newman, K. & Fan, X. Improved Finite Element Modeling of Moisture Diffusion Considering Discontinuity at Material Interfaces in Electronic Packages. in *2019 IEEE 69th Electronic Components and Technology Conference (ECTC)* 806–810 (IEEE, 2019). <https://doi.org/10.1109/ECTC.2019.00127>.
 40. Chen, L., Zhou, J., Chu, H., Zhang, G. & Fan, X. Modeling nonlinear moisture diffusion in inhomogeneous media. *Microelectron. Reliab.* **75**, 162–170 (2017).

Acknowledgements

This work was supported by the Korean government (the Ministry of Science and ICT, the Ministry of Trade, Industry, and Energy, the Ministry of Health & Welfare, and the Ministry of Food and Drug Safety). (Nos. 2022R1C1C101007112, RS-2023-00221295, HR22C183201, RS-2020-KD000093, RS-2023-00234581, 23-SENS-01).

Author contributions

S.J. Yoon and J. Ha equally contributed to the work. S.J. Yoon and J. Ha contributed to the investigation, validation, data curation, and visualization, and B.H. Lee, J.T. Park, and H. Lee contributed to data acquisition from experiments. A. Yang and K.-I. Jang contributed to formal analysis, and methodology. Y.K. Lee contributed to conceptualization, writing, supervision, and funding acquisition. All authors reviewed and commented on the paper before publication.

Competing interests

The authors declare no competing interests.

Additional information

Supplementary information The online version contains supplementary material available at

<https://doi.org/10.1038/s41528-024-00308-0>.

Correspondence and requests for materials should be addressed to Yoon Kyeung Lee.

Reprints and permissions information is available at <http://www.nature.com/reprints>

Publisher's note Springer Nature remains neutral with regard to jurisdictional claims in published maps and institutional affiliations.

Open Access This article is licensed under a Creative Commons Attribution 4.0 International License, which permits use, sharing, adaptation, distribution and reproduction in any medium or format, as long as you give appropriate credit to the original author(s) and the source, provide a link to the Creative Commons licence, and indicate if changes were made. The images or other third party material in this article are included in the article's Creative Commons licence, unless indicated otherwise in a credit line to the material. If material is not included in the article's Creative Commons licence and your intended use is not permitted by statutory regulation or exceeds the permitted use, you will need to obtain permission directly from the copyright holder. To view a copy of this licence, visit <http://creativecommons.org/licenses/by/4.0/>.

© The Author(s) 2024